IJMMM International Journal of Minerals, Metallurgy and Materials 矿物冶金与材料学报（英文版）

Construction of attapulgite-based one-dimensional nanonetwork composites with corrosion resistance for high-efficiency microwave absorption

Kai Xu, Qingqing Gao, Shaoqi Shi, Pei Liu, Yinxu Ni, Zhilei Hao, Gaojie Xu, Yan Fu, and Fenghua Liu

Cite this article as:
Kai Xu, Qingqing Gao, Shaoqi Shi, Pei Liu, Yinxu Ni, Zhilei Hao, Gaojie Xu, Yan Fu, and Fenghua Liu, Construction of attapulgite-based one-dimensional nanonetwork composites with corrosion resistance for high-efficiency microwave absorption, *Int. J. Miner. Metall. Mater.*, 32(2025), No. 3, pp. 689-698. https://doi.org/10.1007/s12613-024-2917-5

Articles you may be interested in

Yuanchun Zhang, Shengtao Gao, Xingzhao Zhang, Dacheng Ma, Chuanlei Zhu, and Jun He, Structural and microwave absorption properties of $CoFe_2O_4$/residual carbon composites, *Int. J. Miner. Metall. Mater.*, 32(2025), No. 1, pp. 221-232. https://doi.org/10.1007/s12613-024-2849-0

Bowei Zhang, Qiao Zhang, Zhan Zhang, Kui Xiao, Qiong Yao, Guojia Ma, Gang Sun, and Junsheng Wu, Incorporation of nano/micron-SiC particles in Ni-based composite coatings towards enhanced mechanical and anti-corrosion properties, *Int. J. Miner. Metall. Mater.*, 29(2022), No. 1, pp. 153-160. https://doi.org/10.1007/s12613-021-2307-1

Yahui Wang, Minghui Zhang, Xuesong Deng, Zhigang Li, Zongsheng Chen, Jiaming Shi, Xijiang Han, and Yunchen Du, Reduced graphene oxide aerogel decorated with Mo_2C nanoparticles toward multifunctional properties of hydrophobicity, thermal insulation and microwave absorption, *Int. J. Miner. Metall. Mater.*, 30(2023), No. 3, pp. 536-547. https://doi.org/10.1007/s12613-022-2570-9

Qiang Su, Hanqun Wang, Yunfei He, Dongdong Liu, Xiaoxiao Huang, and Bo Zhong, Preparation of CIP@TiO_2 composite with broadband electromagnetic wave absorption properties, *Int. J. Miner. Metall. Mater.*, 31(2024), No. 1, pp. 197-205. https://doi.org/10.1007/s12613-023-2707-5

Lianggui Ren, Yiqun Wang, Xin Zhang, Qinchuan He, and Guanglei Wu, Efficient microwave absorption achieved through *in situ* construction of core–shell $CoFe_2O_4$@mesoporous carbon hollow spheres, *Int. J. Miner. Metall. Mater.*, 30(2023), No. 3, pp. 504-514. https://doi.org/10.1007/s12613-022-2509-1

Guomin Li, Xiaojie Xue, Lutao Mao, Yake Wang, Lingxiao Li, Guizhen Wang, Kewei Zhang, Rong Zhang, Yuexiang Wang, and Liping Liang, Recycling and utilization of coal gasification residues for fabricating Fe/C composites as novel microwave absorbents, *Int. J. Miner. Metall. Mater.*, 30(2023), No. 3, pp. 591-599. https://doi.org/10.1007/s12613-022-2534-0

IJMMM WeChat

QQ author group

INTERNATIONAL JOURNAL OF
Minerals, Metallurgy and Materials

Volume 32, Number 3, March 2025
Page 689

Research Article

https://doi.org/10.1007/s12613-024-2917-5

Construction of attapulgite-based one-dimensional nanonetwork composites with corrosion resistance for high-efficiency microwave absorption

Kai Xu[1,2], *Qingqing Gao*[2], *Shaoqi Shi*[2], *Pei Liu*[2], *Yinxu Ni*[2], *Zhilei Hao*[2], *Gaojie Xu*[2], *Yan Fu*[3], *and Fenghua Liu*[2]✉

1) School of Materials Science and Chemical Engineering, Ningbo University, Ningbo 315211, China

2) Zhejiang Key Laboratory of Additive Manufacturing Materials, Ningbo Institute of Materials Technology & Engineering, Chinese Academy of Sciences, Ningbo 315201, China

3) Northwest Yongxin Coatings Limited Company, Lanzhou 730046, China

(Received: 15 February 2024; revised: 15 April 2024; accepted: 17 April 2024)

Abstract: Exploring high-efficiency and broadband microwave absorption (MA) materials with corrosion resistance and low cost is urgently needed for wide practical applications. Herein, the natural porous attapulgite (ATP) nanorods embedded with TiO_2 and polyaniline (PANI) nanoparticles are synthesized via heterogeneous precipitation and *in-situ* polymerization. The obtained PANI–TiO_2–ATP one-dimensional (1D) nanostructures can intertwine into three-dimensional (3D) conductive network, which favors energy dissipation. The minimum reflection loss (RL_{min}) of the PANI–TiO_2–ATP coating (20wt%) reaches −49.36 dB at 9.53 GHz, and the effective absorption bandwidth (EAB) can reach 6.53 GHz with a thickness of 2.1 mm. The excellent MA properties are attributed to interfacial polarization, multiple loss mechanisms, and good impedance matching induced by the synergistic effect of PANI–TiO_2 nanoparticle shells and ATP nanorods. In addition, salt spray and Tafel polarization curve tests reveal that the PANI–TiO_2–ATP coating shows outstanding corrosion resistance performance. This study provides a low-cost and high-efficiency strategy for constructing 1D nanonetwork composites for MA and corrosion resistance applications using natural porous ATP nanorods as carriers.

Keywords: microwave absorption; corrosion resistance; attapulgite; TiO_2; polyaniline

1. Introduction

With the development of wireless communications and radar detection technologies, the increasing electromagnetic (EM) pollution and interference have become a serious problem to human health and facility operations [1–3]. Consequently, more and more attention has been paid to microwave absorption (MA) materials used in EM protection, information security, and stealth technology [4–6]. Generally, the design and fabrication of MA materials mainly focus on the selection of proper elements and the construction of specific structures [7–10]. With the widespread application of microwave wireless communications technology in more fields, the new EM environments have put forward higher demand for the performance of MA materials [11–13]. The overall requirements of "thin, light, wide, and strong" and excellent environmental adaptability for single-phase absorption materials are difficult to achieve [14–16]. The combination of dielectric oxide and conductive materials has been proven to be a promising strategy for fabricating more efficient microwave absorbers. This strategy enables the composite materials to inherit the loss properties from their individual components, adjust their EM parameters, and improve the impedance matching, which are conducive to manufacturing high-performance and multifunctional MA materials [14–15,17–18].

In addition, the microstructure also has a significant influence on the MA performance [19–23]. Recently, many studies focus on dimensional design and core–shell engineering to construct efficient absorbers [24–26]. Bhattacharya *et al.* [27] used hexadecyl trimethyl ammonium bromide (CTAB) binder to combine TiO_2–WNCNT (multi wall carbon nanotube) with polyaniline (PANI) to prepare the supported interlayer structure, achieving an optimal reflection loss (RL) performance of −60 dB. According to the latest research, one-dimensional (1D) core–shell MA-related materials, benefiting from anisotropy and high aspect ratio, are prone to form a carrier transport path in the axial direction under EM fields, which consumes the energy of EM waves through multiple losses [27–28]. Liu *et al.* [29] prepared 1D short-rod materials by coating TiO_2 onto Co–Fe. TiO_2 provided an additional conduction loss and polarization loss for the material, resulting in an effective absorption bandwidth of −51.5 dB and an effective absorption bandwidth (EAB) of 8.6 dB. In addition, the 1D materials possess spatial confinement effect, quantum tunneling effect, and shape anisotropy, breaking

✉ Corresponding author: Fenghua Liu E-mail: lfh@nimte.ac.cn

through the limits of isotropic materials, which are promised to be beneficial for MA [30–31].

However, most of the current 1D core–shell MA materials are constructed using artificial synthetic fibers as carriers, and their fabrication is generally relatively complex, requiring specific conditions and complex processes, which still have limitations for wider applications [32–33]. Furthermore, in an actual environment, metal corrosion and spalling of the coat will reduce the MA performance. Therefore, improving the corrosion resistance of MA materials is both necessary and important [13,22,34].

In this work, the natural porous 1D nanometer material attapulgite (ATP) with low price, suitable size, high aspect ratio, and stable structure was used as a carrier to construct the novel 1D core–shell structure PANI–TiO_2–ATP nanonetwork composite via versatile kinetics-controlled coating method and *in-situ* polymerization [32,35–36]. The minimum reflection loss (RL_{min}) of the obtained 1D core–shell structure PANI–TiO_2–ATP coating (20wt%) reached −49.36 dB at 9.53 GHz, and the EAB extended to 6.53 GHz with a thickness of 2.1 mm. The excellent MA properties are attributed to interfacial polarization, multiple losses, and good impedance matching induced by the synergistic effect of PANI–TiO_2 nanoparticle shells and ATP nanorods. In addition, salt spray and Tafel polarization curve tests revealed that the PANI–TiO_2–ATP coating exhibits outstanding corrosion resistance performance. This study provides a low-cost and high-efficiency strategy for constructing 1D nanonetwork composites for MA and corrosion resistance applications using natural porous ATP nanorods as carriers.

2. Experimental

2.1. Materials

ATP was provided by Jiangsu Jiuchuan Nanometer Material Co. Ltd. from China. Ammonium persulfate (APS), aniline, and tetrabutyl titanate were purchased from Aladdin Chemical Reagent Co., Ltd., China. Aqueous ammonia ($NH_3{\cdot}H_2O$, 25%–28%) and concentrated hydrochloric acid (HCl, 33%–36%) were purchased from Sinopharm Chemical Reagent Co., Ltd., China.

2.2. Preparation of TiO_2–ATP

TiO_2–ATP nanoparticles were synthesized through a versatile kinetics-controlled coating method [37–38]. First, solution A was prepared by mixing 50 mL of absolute ethanol with 5 mL of tetrabutyl titanate under magnetic stirring for 30 min. Then, 1 g of ATP and 1.6 mL of $NH_3{\cdot}H_2O$ were combined with 350 mL of absolute ethanol under magnetic stirring for 1 h named solution B. Solution A was then slowly dripped into the solution B under magnetic stirring for 24 h. Finally, the mixed solutions were subsequently washed three times with absolute ethanol and deionized water and then dried at 90°C for 8 h.

2.3. Synthesis of PANI–TiO_2–ATP

PANI–TiO_2–ATP nanonetwork composites were synthesized through *in-situ* polymerization using TiO_2–ATP nanoparticles and aniline as raw materials. First, 50 mL of HCl solution (1 mol/L) was added to 00 mL beaker and stirred for 15 min at 0–5°C. Then, 0.5 g of TiO_2–ATP powders and 25 mmol of APS were added to the beaker. Afterwards, 25 mmol of aniline was slowly added to the mixed solution and mechanically stirred for 4 h at 0–5°C. Finally, green powders were collected via vacuum filtration, followed by washing three times with deionized water and absolute ethanol. Green powders were dried at 90°C for 8 h, and the resulting product is denoted as PANI–TiO_2–ATP.

2.4. Characterization

Microscopic morphology was characterized by field emission scanning electron microscopy (FE-SEM, Hitachi Limited, S4800). Crystal structures were characterized by X-ray diffractometry (XRD, Shimadzu, LabX XRD-6000). Reflection studies were carried out using PE Lambda 950 instrument. EM parameters were measured using Agilent E8363B instrument. Anticorrosion properties were measured with ModuLab.

3. Results and discussion

3.1. Synthesis mechanism of PANI–TiO_2–ATP

TiO_2–ATP nanoparticles were synthesized through a versatile kinetics-controlled coating method [22]. Tetrabutyl titanate easily undergoes hydrolysis with water, and the reaction formula is shown below [38]:

Hydrolysis:

$$\begin{array}{c} | \\ -\mathrm{Ti}- \\ | \end{array} \mathrm{OC_4H_9} + \mathrm{H_2O} \rightarrow \begin{array}{c} | \\ -\mathrm{Ti}- \\ | \end{array} \mathrm{OH} + \mathrm{C_4H_9OH} \quad (1)$$

Condensation:

$$\begin{array}{c} | \\ -\mathrm{Ti}- \\ | \end{array} \mathrm{OH} + \begin{array}{c} | \\ -\mathrm{Ti}- \\ | \end{array} \mathrm{OH} \rightarrow \begin{array}{c} | \\ -\mathrm{Ti}- \\ | \end{array} \mathrm{O} \begin{array}{c} | \\ -\mathrm{Ti}- \\ | \end{array} + \mathrm{H_2O} \quad (2)$$

Li *et al*. [37] used a versatile kinetics-controlled method to precisely control the growth of the TiO_2 shell, which can be precisely controlled the Fe_3O_4 and SiO_2. $NH_3{\cdot}H_2O$ is the key influencing factor that controls the nucleation mode throughout the experiment. The more $NH_3{\cdot}H_2O$ used in the same period, the thicker the TiO_2 layer generated by heterogeneous nucleation. As the amount of $NH_3{\cdot}H_2O$ increases, the speed of homogeneous nucleation exceeds that of heterogeneous nucleation, and TiO_2 tends to spheroidize rather than form a shell on the carrier. Similarly, precise control of the TiO_2 layer thickness on ATP was achieved [38]. When the amount of $NH_3{\cdot}H_2O$ is 1.6 mL, obviously, the TiO_2 layer will be produced on the ATP surface. In contrast, when the amount of $NH_3{\cdot}H_2O$ reaches 2.8 mL, homogeneous nucleation is dominant, resulting in the spherical TiO_2. In this work, due to slight differences in ATP types, the overall amount of $NH_3{\cdot}H_2O$ is controlled between 1.2 and 2.0 mL to

maintain the heterogeneous nucleation and growth of TiO_2 on the ATP surface.

Fig. 1 shows the synthesis process for PANI–TiO_2–ATP. 1D PANI–TiO_2–ATP nanonetwork composites were synthesized through *in-situ* polymerization using TiO_2–ATP nanoparticles and aniline as raw materials [4]. TiO_2–ATP is rich in Ti–OH, Si–OH, and Mg–OH groups and has a negative charge [5–6]. An acidic environment will activate these groups to enhance the bonding within the reaction. Aniline and APS will react in acidic environment to produce pure PANI with positive charge and short-rod-like shape [8]. Interestingly, during the growth process, positively charged PANI will be attracted by negatively charged ATP and lead to PANI shell through electrostatic self-assembly [9–10]. Strong agglomeration will happen in ATP nanorods due to the rich groups [11]. However, the dispersion of ATP in acidic solution during the *in-situ* growth enables the van der Waals force to prevail over the agglomeration force [12]. Continuous mechanical stirring offers better dispersion and keeps the distance between each ATP rod [13]. This distance provides temporary 3D nanonetwork structure formed by ATP rods [14–15]. Then, the growth of the PANI shell will be a priority to cover TiO_2–ATP compared with the growth of PANI short-rods and fasten the temporary network of ATP [16].

3.2. Microstructure and chemical composition

Fig. 2 shows the microstructure of the different samples. According to Fig. 2(a), ATP has a rod-like structure with lengths in the range of 1–1.5 μm [17]. The crystal structure of

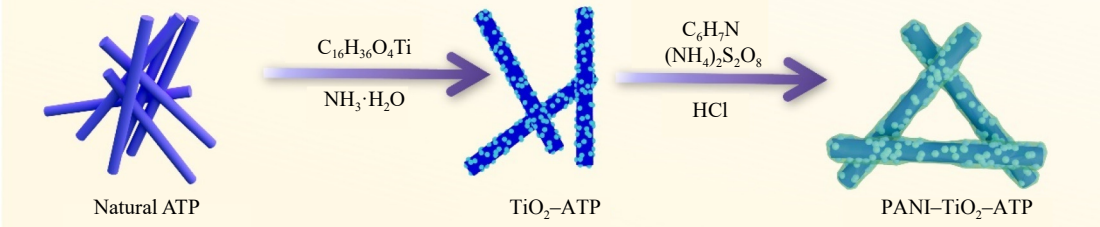

Fig. 1. Illustration of the synthesis process for PANI–TiO_2–ATP.

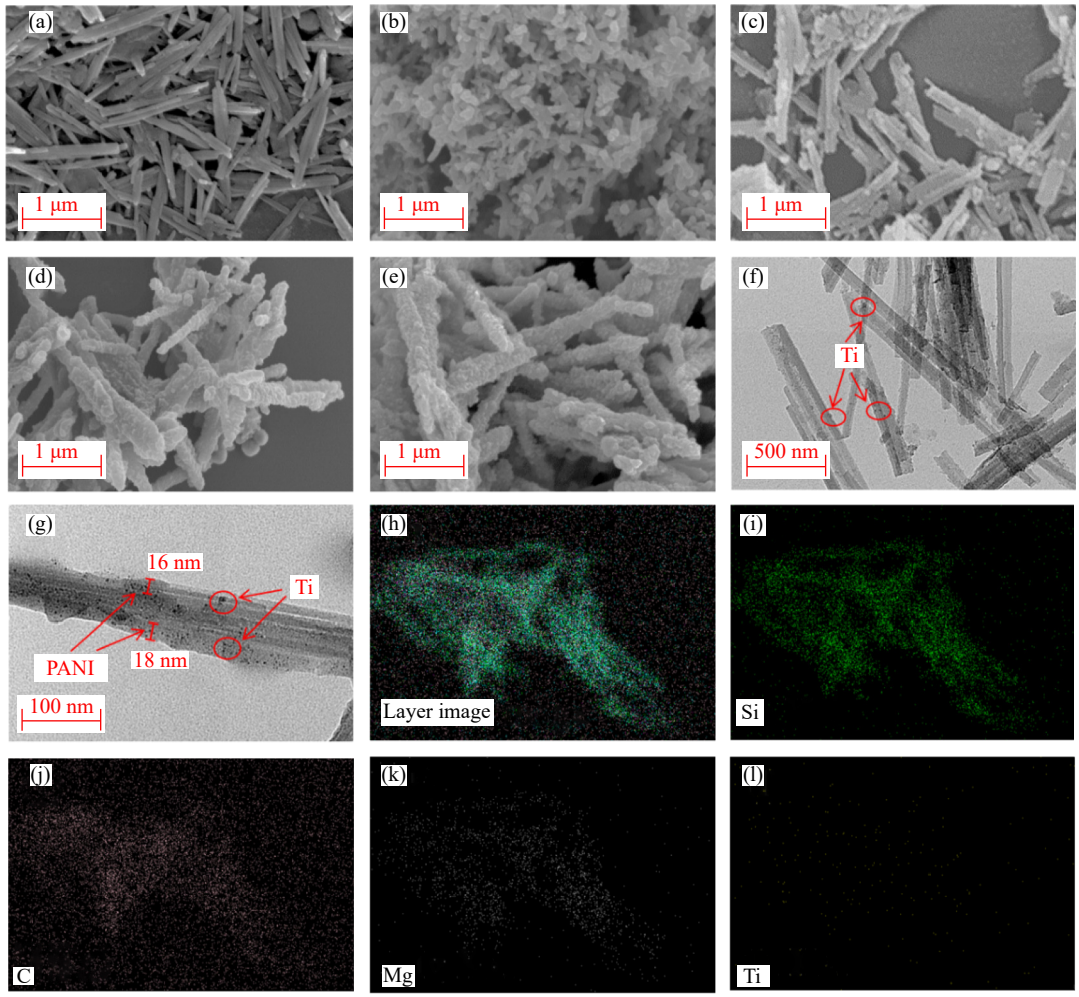

Fig. 2. SEM images of (a) ATP, (b) PANI, (c) TiO_2–ATP, (d) PANI–ATP, and (e) PANI–TiO_2–ATP. TEM images of (f) TiO_2–ATP and (g) PANI–TiO_2–ATP. EDS elemental mapping images of PANI–TiO_2–ATP: (h) layer image; (i) Si; (j) C; (k) Mg; (l) Ti.

ATP is characterized by two Si–O tetrahedron bonds along the *c* axis, and the oxygen atoms will be the apex to link other Si–O tetrahedron bonds along the same direction. Other metal atoms will scatter around the *c* axis and common atoms including Al and Fe [18]. The residue apex will connect with the –OH bonds. Fig. 2(b) shows pure PANI with the shape of smoother short rods and obviously shorter aspect ratio than ATP. The XRD pattern (Fig. S1, see the supplementary information) of pure PANI has obvious peaks at 18° and 26°, corresponding to the (020) and (200) of PANI (JCPDS No. 10-0325), respectively [19]. Fig. 2(c) illustrates ATP rods loaded with rough shell of amorphous TiO_2. The XRD pattern of TiO_2–ATP shows halo peak from 10° to 20°, indicating that an amorphous TiO_2 shell is successfully loaded at the surface of ATP [2]. The PANI shell-covered ATP has significantly changed the diameters of rods and given graininess surface. Fig. 2(d) and (e) shows few differences in shape or surface morphology. PANI–TiO_2–ATP has a halo peak, which corresponds to the (231) of ATP according to the XRD pattern, which indicates that PANI and amorphous TiO_2 had successfully loaded at the surface of ATP. As shown in Fig. 2(l) and Fig. S2, TiO_2 is mainly loaded on the surface of ATP in the form of particles, and the thickness of the loaded layer is relatively thin. Si and Mg elemental mapping images clearly show the rod structure of ATP. During the PANI loading process, TiO_2 will partially dissolve due to HCl and participate in the formation of the PANI–TiO_2 shell on the ATP surface. The Ti elements obviously decrease after synthesis of the PANI shell, but the Ti elements still distribute along the ATP rod. As shown in Fig. 2(g), the thickness of the PANI layer is 16 nm, and TiO_2 distributes within it. The C elemental mapping image (Fig. 2(j)) shows that PANI successfully covered the rod. This indicates the formation of a core–shell structure with the PANI–TiO_2 layer coating the ATP. Notably, PANI–TiO_2–ATP rods reduced the agglomeration effect and formed 3D network.

3.3. EM wave absorption mechanism

Fig. 3 shows the dielectric properties of the ATP, PANI, TiO_2–ATP, PANI–ATP, and PANI–TiO_2–ATP samples. According to the classical theory, RL and impedance usually represent the MA performance of materials [20], which can be calculated according to the following formulas [21–22]:

$$Z_{in} = Z_0 \sqrt{\frac{\mu_r}{\varepsilon_r}} \tanh\left(j\frac{2\pi}{c}\sqrt{\mu_r\varepsilon_r} f d\right) \tag{3}$$

$$RL\,(dB) = 20\lg\left|\frac{Z_{in}-1}{Z_{in}+1}\right| \tag{4}$$

where Z_{in}, Z_0, and d are the input impedance, free impedance, and thickness of the absorber, respectively, ε_r and μ_r are the relative permittivity and permeability of the absorber, respectively, c is the speed of light, f represents the frequency of the electromagnetic wave, and $j^2 = -1$.

Fig. 3(a) and (b) shows the real permittivity (μ') and imaginary permittivity (μ'') of ATP, PANI, TiO_2–ATP, PANI–ATP, and PANI–TiO_2–ATP. Pure PANI shows the highest μ' and μ'' among all materials, but an excessively high electric ability will break the impedance matching (Z) that will reduce the absorption ability of microwaves. According to previous work, an amorphous TiO_2 shell was introduced to balance the impedance matching by reducing the electric ability [23] and providing core–shell structure for additional loss mechanism. PANI composite materials show slightly weaker performance than PANI and obvious improvement compared with ATP and TiO_2–ATP. According to Fig. 3(c), PANI, PANI–ATP, and PANI–TiO_2–ATP show more higher electric loss than pure ATP and TiO_2–ATP. The change in PANI composite electrical performance is beneficial for subsequent impedance matching. The improvement of electric performance also indicates that PANI is successfully connected with ATP and TiO_2–ATP.

Fig. 3(d) and (e) shows the real part of permeability and the imaginary part of permeability of the materials. ATP has the highest μ'' and μ' among all materials. The amorphous TiO_2 shell has a limited influence on magnetic ability. Although the electric performance of ATP and TiO_2–ATP is poor, they show better magnetic performance than PANI composites (Fig. 3(f)).

Fig. 4 shows the illustration of the potential microwave loss mechanism of PANI–TiO_2–ATP. Imaginary permittivity (μ'') and imaginary permeability (ε'') have a significant influence on MA ability. Real permittivity (μ') and real permeability (ε') have an influence on storage ability [24–25]. In this work, the conductive polymer PANI was introduced to adjust impedance matching and enhance electric performance to provide more loss mechanization, such as conduction loss, interfacial polarization, and dipole polarization.

3.4. EM wave absorption performance

Fig. 5 shows the RL, EAB, and thickness of ATP, PANI, TiO_2–ATP, PANI–ATP, and PANI–TiO_2–ATP. Fig. S3(a)–(c) exhibits the RL performance of the samples prepared via a versatile kinetics-controlled coating method with the addition of 1.2, 1.6, and 2.0 mL of $NH_3{\cdot}H_2O$, which are named as 1.2-TiO_2–ATP, 1.6-TiO_2–ATP, and 2-TiO_2–ATP, respectively. The results indicate that TiO_2–ATP exhibits effective EM absorption performance with an RL_{min} of −17.84 dB and EAB of 4.01 GHz when the $NH_3{\cdot}H_2O$ addition amount is 1.6 mL. The samples prepared by *in-situ* polymerization using TiO_2–ATP as a carrier with the addition of 20, 25, and 30 mmol of aniline are named as 20-PANI–TiO_2–ATP, 25-PANI–TiO_2–ATP, and 30-PANI–TiO_2–ATP, respectively. During the PANI loading process, TiO_2 will partially dissolve due to HCl and participate in the formation of the PANI–TiO_2 shell on the ATP surface. It is difficult to effectively adjust the impedance and provide dielectric loss with a small amount of TiO_2, while too much TiO_2 leads to increased spheroidization and damages the microscopic 3D network. As shown in Fig. S3(d)–(f), 25-PANI–TiO_2–ATP achieves the best EM absorption performance. Therefore, 1.6 mL of $NH_3{\cdot}H_2O$ and 25 mmol of aniline were the key parameters to prepare PANI–TiO_2–ATP composite materials.

As shown in Fig. 5(a), (c), and (e), the RL performance of

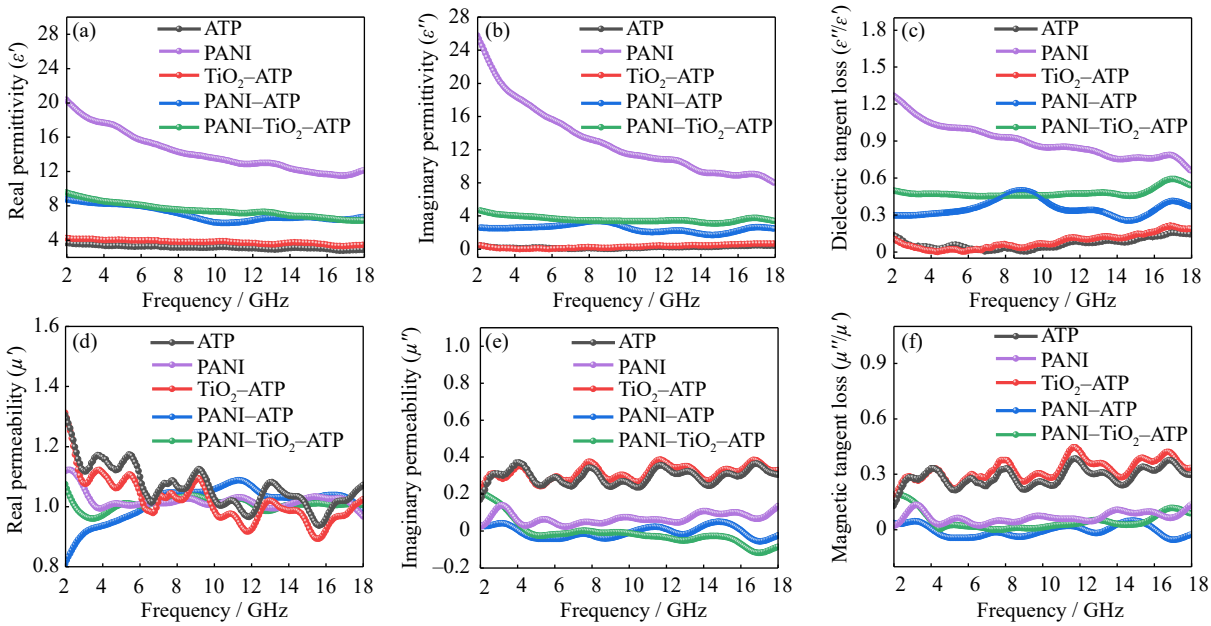

Fig. 3. Dielectric property curves of the samples: (a) ε'; (b) ε''; (c) tanδ_ε'; (d) μ; (e) μ''; (f) tanδ_μ.

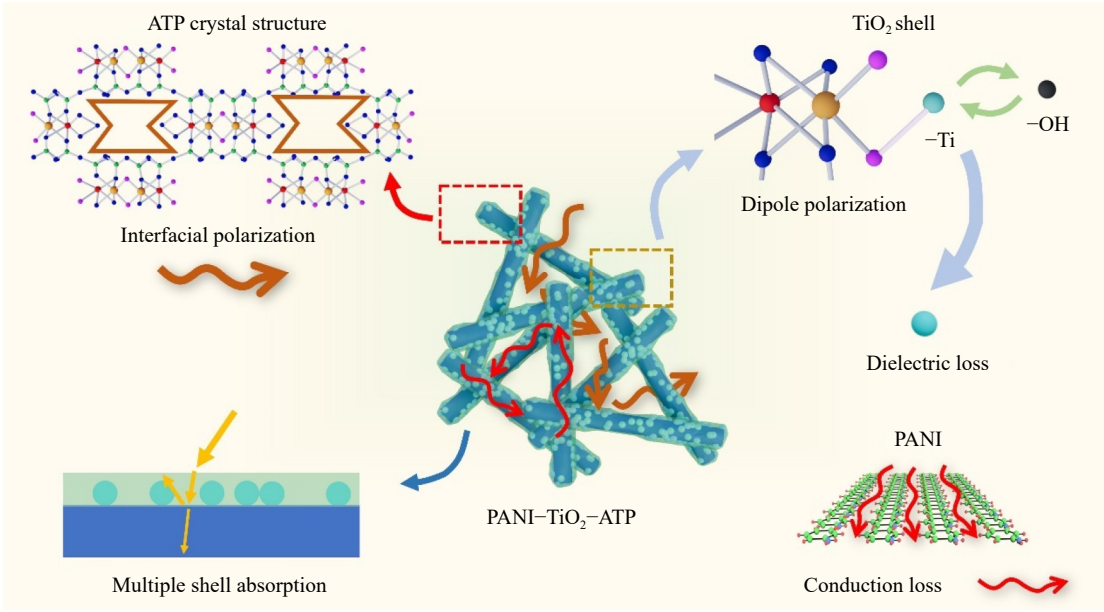

Fig. 4. Illustration of the potential microwave loss mechanism of PANI–TiO_2–ATP.

ATP, PANI, and TiO_2–ATP only reaches the maximum of −17.84 dB. These three materials exhibit poor EM wave absorption performance alone, as shown in Fig. 3. This leads to poor impedance matching and difficulty in obtaining good EM wave absorption properties. Therefore, this work combined ATP, amorphous TiO_2, and PANI to enrich the EM wave loss mechanism and adjust impedance matching.

In Fig. 5(g), PANI–ATP achieves RL of −30.08 dB and effective bandwidth of 3.52 GHz. Although the enhancement is not significant, the complex formation of the core–shell structure by PANI and ATP enriches the RL mechanism. Meanwhile, PANI–TiO_2–ATP has the best RL of −49.28 dB and the best effective bandwidth of 6.53 dB (Fig. 5(i)). Compared with the other four materials, there is a significant improvement in both RL and effective bandwidth.

3.5. Impedance matching

Impedance matching (Z) and attenuation constant (α) are very important factors for EM wave absorption. As the impedance matching at the interface between the ideal medium and the object becomes close to 1, the microwaves are more prone to get into materials and facilitate the operation of the loss mechanism. Also, high attenuation constant (α) will reduce residual EM waves. The expression for α is as follows [30–31]:

$$\alpha = \frac{\sqrt{2\mu'\varepsilon'} \times \pi f}{c} \times \sqrt{(\tan\delta_\varepsilon \tan\delta_\mu - 1) + \sqrt{(\tan\delta_\varepsilon \tan\delta_\mu - 1)^2 + (\tan\delta_\varepsilon + \tan\delta_\mu)^2}} \quad (5)$$

Fig. 6(a)–(f) shows the impedance matching and attenu-

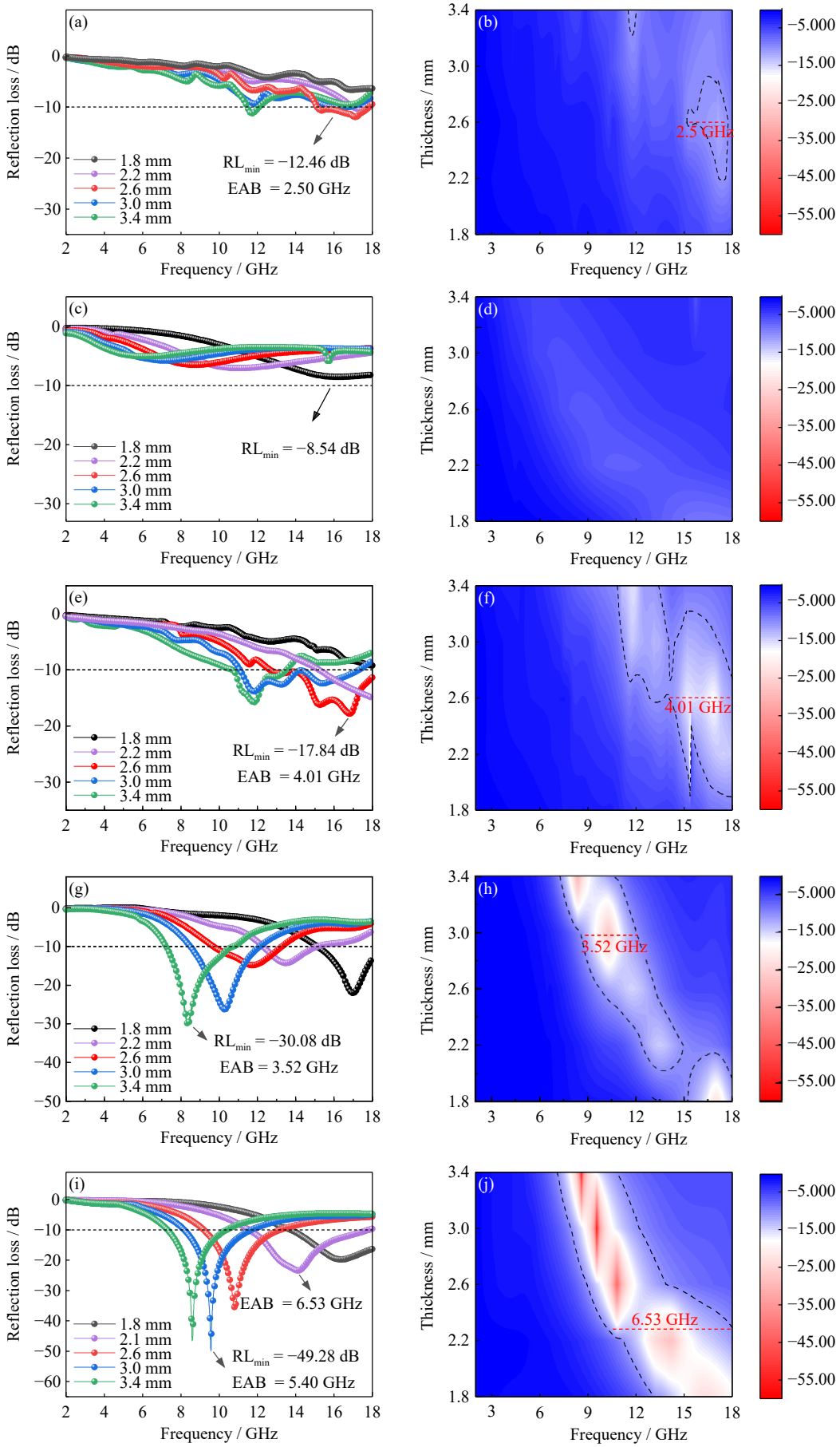

Fig. 5. RL curves and projection drawings of (a, b) ATP, (c, d) PANI, (e, f) TiO_2–ATP, (g, h) PANI–ATP, and (i, j) PANI–TiO_2–ATP.

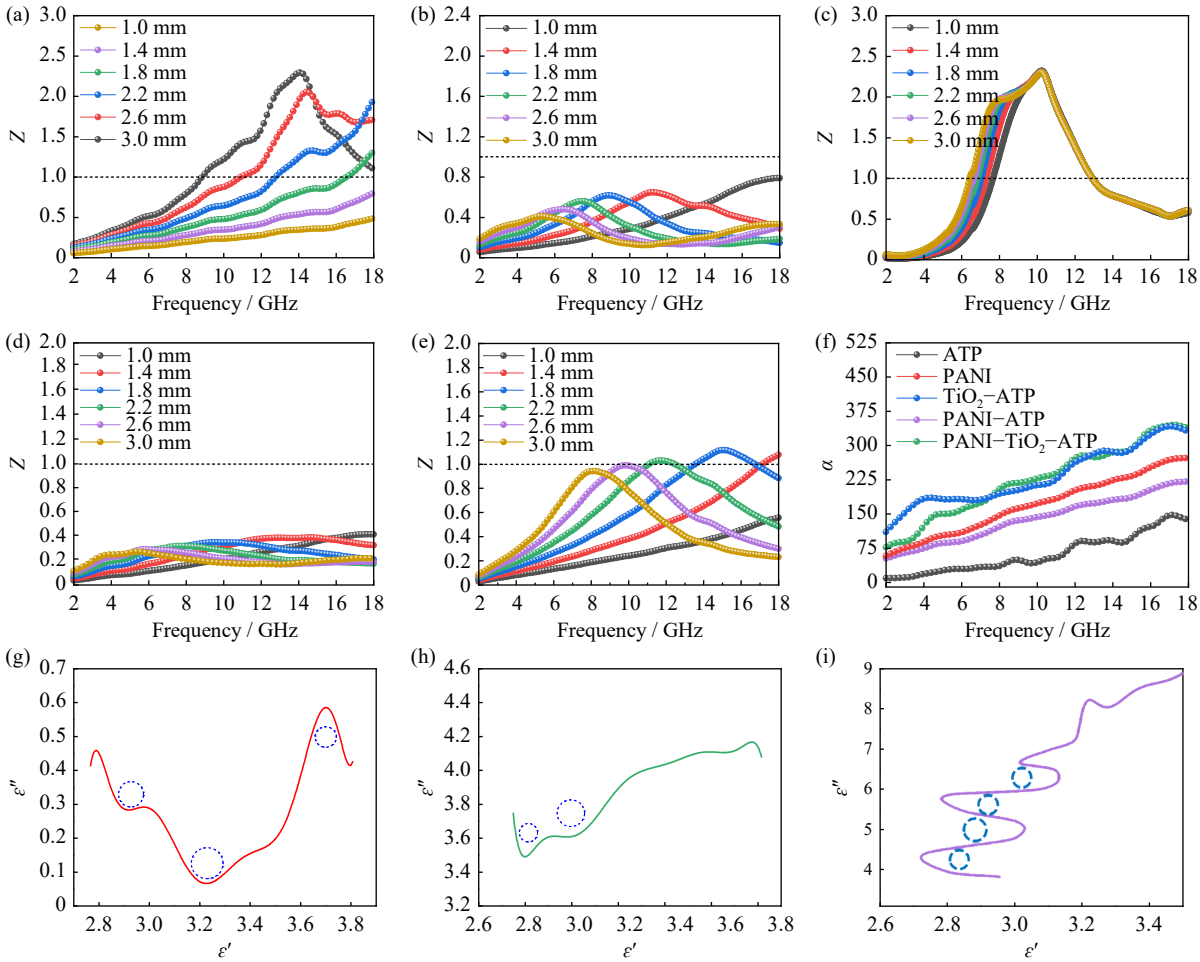

Fig. 6. Impedance matching (*Z*) curves of (a) ATP, (b) TiO_2–ATP, (c) PANI, (d) PANI–ATP, and (e) PANI–TiO_2–ATP. (f) Attenuation constant (α) of samples. Cole–Cole plots of (g) ATP, (h) PANI–ATP, and (i) PANI–TiO_2–ATP.

ation constant of the different materials at different thicknesses. According to Fig. 6(a) and (c), ATP and PANI show significant deviations from the ideal impedance matching (Z = 1) [24,32], which is consistent with Fig. 3. Fig. 6(b) shows that the incorporation of amorphous TiO_2 plays a significant moderating role in the impedance matching imbalance of ATP, reducing the impedance error from up to 100% to within 20%. Furthermore, TiO_2 will balance the runaway impedance matching by reducing conductivity. The thickness of the material varied from 1.8 to 3.4 mm, with small changes in impedance matching. However, good impedance matching brings only a small improvement in RL performance. As shown in Fig. 6(e), PANI–TiO_2–ATP exhibits significant RL and effective width enhancement approaching the ideal impedance Z = 1.

Fig. 6(f) shows the attenuation constant (α) curves for different materials. The values of α are ordered as PANI > PANI–ATP > PANI–TiO_2–ATP > TiO_2–ATP > ATP. The higher the value of α is, the stronger the conductive loss is.

However, effective bandwidth and efficient RL require more complex loss mechanisms [33]. The Debye theory can effectively analyze the interfacial polarization effects and the Cole–Cole curves is the most effective representations of the Debye theory. Cole–Cole curves can have numerous burrs that make analysis more difficult. Therefore, when analyzing the effect of interface polarization, only the obvious large curvature parts are selected [34–35], and the formula is shown below [36]:

$$\left(\varepsilon' - \frac{\varepsilon_s + \varepsilon_\infty}{2}\right)^2 + (\varepsilon'')^2 = \left(\frac{\varepsilon_s - \varepsilon_\infty}{2}\right)^2 \quad (6)$$

where ε_s and ε_∞ represent the static permittivity and complex permittivity, respectively.

As shown in the Cole–Cole curves in Fig. 6(g), ATP is a naturally occurring nanorod-like material with natural channels, which confers an advantage via rich interfacial polarization to the material. There are three obvious curvature circles in the Cole–Cole curves. The combination of PANI and ATP improves the overall impedance matching, but the covering of ATP by the PANI shells concurrently weakens the interfacial polarization (Fig. 6(h)). The early intervention of amorphous TiO_2 has a limited effect on the overall impedance matching. According to previous work, the amorphous TiO_2 not only effectively attenuates the high dielectric properties of PANI but also preserves the natural channels of ATP during the formation of a porous layer. In Fig. 6(i), amorphous TiO_2 is specifically characterized by numerous large-angle curvature circles. This indicates that PANI–TiO_2–ATP possesses rich interfacial polarization effects.

3.6. Anticorrosion property

Fig. 7 shows the corrosion resistance of the steel surface after 0 and 1000 h salt spray tests for A235 steel, ATP, TiO_2–ATP, and PANI–TiO_2–ATP. In the 0 h salt spray test, the A235 steel surface was bright, but after 1000 h, there were large corrosion marks on the surface. The scratches are especially obvious in the case of vandalism X and tend to corrode outward. ATP, TiO_2–ATP, and PANI–TiO_2–ATP showed obvious color differences (yellow, yellow-white, and black). As can be seen in Fig. 7(b)–(d), it can be found that the ATP film and PANI–TiO_2–ATP have obvious granularity on the surface, while the TiO_2–ATP surface is smoother. After 1000 h salt spray test, ATP, TiO_2–ATP, and PANI–TiO_2–ATP showed obvious corrosion resistance. The corrosion is mainly at the X-scratches and has a small tendency to spread outward, and the diffusion area of TiO_2–ATP is enlarged compared to that of ATP. Notably, the PANI–TiO_2–ATP film formed a clear patchy passivation film on the steel surface. As shown in Fig. 7(i)–(l), corrosion marks became apparent at high-saturation levels.

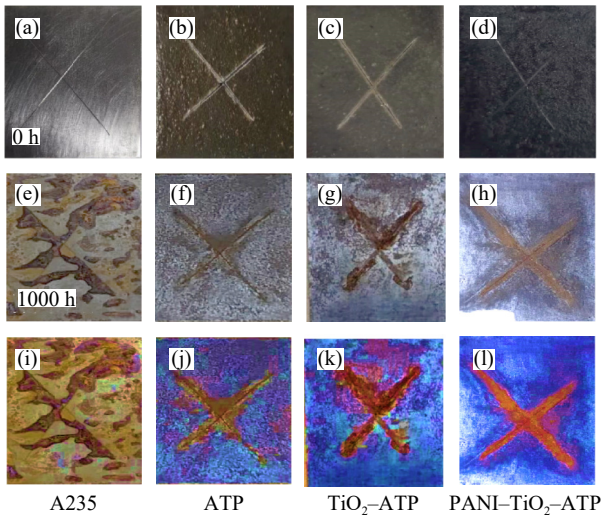

Fig. 7. Photographs of (a, e, i) A235, (b, f, j) ATP, (c, g, k) TiO_2–ATP, and (d, h, l) PANI–TiO_2–ATP coatings after 0 and 1000 h spray salt tests.

Fig. S4 and Table 1 show the polarization curves and electrochemical parameters, respectively. Pure A235-based materials have E_{corr} (corrosion potential) of −0.235 V and low I_{corr} (corrosion current density) of -5.33×10^{-6} A·cm^{-2}. Pure ATP shows similar curves to A235, but with higher I_{corr}, indicating that ATP has less improvement in anticorrosion properties. TiO_2–ATP had higher E_{corr}, indicating the growth of a passivation film during the corrosion, but poor performance at I_{corr} still led to a poor anticorrosion property. PANI–TiO_2–ATP had the lowest I_{corr} and effectively reduced the magnitude of the corrosion current by at least 2 orders of magnitude [19]. The simultaneous fulfillment of conditions, including increased E_{corr} and decreased I_{corr}, will lead to better anticorrosion properties, as shown in Fig. 7(l). From the Nyquist plots in Fig. S4(a), it can be seen that pure ATP and polyurethane films exhibit a distinct turn at low frequencies, indicating the occurrence of significant pitting corrosion and dissolution. In contrast, the pronounced turns for TiO_2–ATP and PANI–TiO_2–ATP occur at higher frequencies [39]. Furthermore, in the impedance modulus curves in Fig. S4(b), TiO_2–ATP and PANI–TiO_2–ATP show an improvement of 2–3 orders of magnitude, indicating a significant enhancement in corrosion resistance. As shown in Fig. S5, the BET surface area of ATP is 115.87 m^2·g^{-1}, which increases to 267.77 m^2·g^{-1} after TiO_2 coating. However, the BET surface area decreases significantly after PANI coating. As shown in Fig. S4(a) and (b), TiO_2–ATP with a high BET surface area shows a slight advantage over PANI–TiO_2–ATP in Nyquist plots and impedance modulus curves and the passivation film is formed earlier. A high specific surface area can optimize corrosion resistance to some extent. However, according to the 1000 h salt test, it is found that PANI–TiO_2–ATP with a low specific surface area has better corrosion resistance. This indicates that the high specific surface area of TiO_2–ATP can accelerate the formation of a passive film, but it has a relatively small impact on improving long-term corrosion resistance. Fig. S5 and Fig. 5 indicate that TiO_2 coating on ATP significantly increases the specific surface area. However, the RL performance only improves by −5.38 dB. Although PANI coating significantly reduces the overall specific surface area, it results in a notable improvement of −17.62 dB in RL. This proves that specific surface area is not a key factor affecting the MA performance of PANI–TiO_2–ATP.

Table 1. Electrochemical parameters obtained by the Tafel polarization curve of A235, ATP, TiO_2–ATP, and PANI–TiO_2–ATP

Materials	E_{corr} / V	I_{corr} / (A·cm^{-2})
A235	−0.230	-5.33×10^{-6}
ATP	−0.245	-3.53×10^{-5}
TiO_2–ATP	−0.089	-1.57×10^{-4}
PANI–TiO_2–ATP	−0.147	-1.43×10^{-8}

The mechanism proposed indicates that the high specific surface area TiO_2–ATP covered by PANI demonstrates remarkable corrosion resistance due to the dual-layer protection mechanism [40]. During the corrosion process, corrosive agents must first penetrate the outer PANI layer before encountering the resistance of the TiO_2–ATP layer. This sequential barrier effect not only ensures exceptional corrosion resistance but also delays the material's degradation, thereby prolonging its durability. In materials science terms, the synergistic effect of the PANI coating and the TiO_2–ATP substrate enhances the material's overall corrosion resistance and longevity [40].

4. Conclusion

In summary, a novel 1D core–shell structure PANI–TiO_2–ATP nanonetwork composite was constructed via a versatile kinetics-controlled coating method and *in-situ* polymerization using natural porous ATP nanorods as carriers.

The obtained 1D core–shell structure PANI–TiO_2–ATP coating (20wt%) shows RL_{min} of −49.36 dB at 9.53 GHz, and the EAB can reach 6.53 GHz at the thickness of 2.1 mm. The excellent MA properties are attributed to interfacial polarization, multiple losses, and good impedance matching induced by the synergistic effect of PANI–TiO_2 nanoparticle shells and ATP nanorods. Furthermore, salt spray and Tafel polarization curve tests reveal that the PANI–TiO_2–ATP coating shows outstanding corrosion resistance performance. This study provides a low-cost and highly efficient strategy for constructing 1D nanonetwork composites for MA and corrosion resistance applications.

Acknowledgements

The authors would like to acknowledge the financial support from the National Key Research and Development Program of China (No. 2021YFB3701503), the Key Research and Development Program of Ningbo, China (No. 2023Z107), the Jiangsu Key R&D program, China (No. BE2019072), and the special project of Gansu regional science and technology cooperation, China (No. 20JR10 QA579).

Conflict of Interest

The authors declare that there is no conflict of interest.

Supplementary Information

The online version contains supplementary material available at https://doi.org/10.1007/s12613-024-2917-5.

References

[1] S. Wang, W. Lian, H.D. Ren, *et al*., Novel composites with a cross-linked polyaniline shell and oriented palygorskite as ideal microwave absorbers, *New J. Chem.*, 45(2021), No. 5, p. 2765.

[2] C. Jin, Z.C. Wu, C.D. Yang, *et al*., Impedance amelioration of coaxial-electrospun TiO_2@Fe/C@TiO_2 vesicular carbon microtubes with dielectric-magnetic synergy toward highly efficient microwave absorption, *Chem. Eng. J.*, 433(2022), art. No. 133640.

[3] L.N. Huang, C.G. Chen, X.Y. Huang, S.C. Ruan, and Y.J. Zeng, Enhanced electromagnetic absorbing performance of MOF-derived Ni/NiO/Cu@C composites, *Composites Part B*, 164(2019), p. 583.

[4] X.F. Shi, Z.W. Liu, X. Li, W.B. You, Z.Z. Shao, and R.C. Che, Enhanced dielectric polarization from disorder-engineered Fe_3O_4@black TiO_{2-x} heterostructure for broadband microwave absorption, *Chem. Eng. J.*, 419(2021), art. No. 130020.

[5] L.X. Li, B.C. Li, L. Fan, B. Mu, A.Q. Wang, and J.P. Zhang, Palygorskite@Fe_3O_4@polyperfluoroalkylsilane nanocomposites for superoleophobic coatings and magnetic liquid marbles, *J. Mater. Chem. A*, 4(2016), No. 16, p. 5859.

[6] H. Zhang, F.F. Yang, Q. Zhang, A.P. Hui, and A.Q. Wang, Structural evolution of palygorskite as the nanocarrier of silver nanoparticles for improving antibacterial activity, *ACS Appl. Bio Mater.*, 5(2022), No. 8, p. 3960.

[7] G.P. Meng, X.J. Mu, L.P. Zhen, *et al*., Confinement and passivation of perovskite quantum dots in porous natural palygorskite toward an efficient and ultrastable light-harvesting system in water, *Chem. Sci.*, 13(2022), No. 47, p. 14141.

[8] M.X. Sun, C. Xu, J.L. Li, *et al*., Protonic doping brings tuneable dielectric and electromagnetic attenuated properties for polypyrrole nanofibers, *Chem. Eng. J.*, 381(2020), art. No. 122615.

[9] Y.L. Zhang and J.W. Gu, A perspective for developing polymer-based electromagnetic interference shielding composites, *Nano Micro Lett.*, 14(2022), No. 1, art. No. 89.

[10] Y. Liao, G.H. He, and Y.P. Duan, Morphology-controlled self-assembly synthesis and excellent microwave absorption performance of MnO_2 microspheres of fibrous flocculation, *Chem. Eng. J.*, 425(2021), art. No. 130512.

[11] C.X. Wang, Y. Liu, Z.R. Jia, W.R. Zhao, and G.L. Wu, Multicomponent nanoparticles synergistic one-dimensional nanofibers as heterostructure absorbers for tunable and efficient microwave absorption, *Nano Micro Lett.*, 15(2022), No. 1, art. No. 13.

[12] B. Mu and A.Q. Wang, Adsorption of dyes onto palygorskite and its composites: A review, *J. Environ. Chem. Eng.*, 4(2016), No. 1, p. 1274.

[13] H.G. Wang, H.S. Ren, C.F. Jing, J.Z. Li, Q. Zhou, and F.B. Meng, Two birds with one stone: Graphene oxide@sulfonated polyaniline nanocomposites towards high-performance electromagnetic wave absorption and corrosion protection, *Compos. Sci. Technol.*, 204(2021), art. No. 108630.

[14] Q.Q. Wang, B. Niu, Y.H. Han, Q. Zheng, L. Li, and M.S. Cao, Nature-inspired 3D hierarchical structured “vine” for efficient microwave attenuation and electromagnetic energy conversion device, *Chem. Eng. J.*, 452(2023), art. No. 139042.

[15] F. Wu, M.X. Sun, W.C. Jiang, *et al*., A self-assembly method for the fabrication of a three-dimensional (3D) polypyrrole (PPy)/poly(3, 4-ethylenedioxythiophene) (PEDOT) hybrid composite with excellent absorption performance against electromagnetic pollution, *J. Mater. Chem. C*, 4(2016), No. 1, p. 82.

[16] J.J. Ding, D.J. Huang, W.B. Wang, Q. Wang, and A.Q. Wang, Effect of removing coloring metal ions from the natural brick-red palygorskite on properties of alginate/palygorskite nanocomposite film, *Int. J. Biol. Macromol.*, 122(2019), p. 684.

[17] W.B. Wang and A.Q. Wang, Recent progress in dispersion of palygorskite crystal bundles for nanocomposites, *Appl. Clay Sci.*, 119(2016), p. 18.

[18] Z. Zhang, J.W. Tan, W.H. Gu, *et al*., Cellulose–chitosan framework/polyailine hybrid aerogel toward thermal insulation and microwave absorbing application, *Chem. Eng. J.*, 395(2020), art. No. 125190.

[19] Z.C. Wu, H.W. Cheng, C. Jin, *et al*., Dimensional design and core–shell engineering of nanomaterials for electromagnetic wave absorption, *Adv. Mater.*, 34(2022), No. 11, art. No. e2107538.

[20] J. Xiong, Z. Xiang, J. Zhao, *et al*., Layered NiCo alloy nanoparticles/nanoporous carbon composites derived from bimetallic MOFs with enhanced electromagnetic wave absorption performance, *Carbon*, 154(2019), p. 391.

[21] Z.Y. Tong, Z.J. Liao, Y.Y. Liu, *et al*., Hierarchical Fe_3O_4/Fe@C@MoS_2 core–shell nanofibers for efficient microwave absorption, *Carbon*, 179(2021), p. 646.

[22] G.L. Wu, Z.R. Jia, X.F. Zhou, G.Z. Nie, and H.L. Lv, Interlayer controllable of hierarchical MWCNTs@C@Fe_xO_y cross-linked composite with wideband electromagnetic absorption performance, *Composites Part A*, 128(2020), art. No. 105687.

[23] H.F. Pang, Y.P. Duan, L.X. Huang, *et al*., Research advances in composition, structure and mechanisms of microwave absorbing materials, *Composites Part B*, 224(2021), art. No. 109173.

[24] M. Zhang, X. Qian, Q.W. Zeng, Y.H. Zhang, H. Cao, and R.C. Che, Hollow microspheres of polypyrrole/magnetite/carbon

nanotubes by spray-dry as an electromagnetic synergistic microwave absorber, *Carbon*, 175(2021), p. 499.
[25] T.Q. Hou, Z.R. Jia, B.B. Wang, *et al*., MXene-based accordion 2D hybrid structure with Co_9S_8/C/$Ti_3C_2T_x$ as efficient electromagnetic wave absorber, *Chem. Eng. J.*, 414(2021), art. No. 128875.
[26] M. Qin, L.M. Zhang, and H.J. Wu, Dielectric loss mechanism in electromagnetic wave absorbing materials, *Adv. Sci.*, 9(2022), No. 10, art. No. e2105553.
[27] P. Bhattacharya, S. Dhibar, M.K. Kundu, G. Hatui, and C.K. Das, Graphene and MWCNT based bi-functional polymer nanocomposites with enhanced microwave absorption and supercapacitor property, *Mater. Res. Bull.*, 66(2015), p. 200.
[28] X.F. Zhou, Z.R. Jia, A.L. Feng, *et al*., Construction of multiple electromagnetic loss mechanism for enhanced electromagnetic absorption performance of fish scale-derived biomass absorber, *Composites Part B*, 192(2020), art. No. 107980.
[29] P.B. Liu, Y.R. Li, H.X. Xu, *et al*., Hierarchical Fe–Co@TiO_2 with incoherent heterointerfaces and gradient magnetic domains for electromagnetic wave absorption, *ACS Nano*, 18(2024), No. 1, p. 560.
[30] W.X. Li, Y.Y. Liu, F. Guo, Y.E. Du, and Y.Q. Chen, Self-assembly sandwich-like Fe, Co, or Ni nanoparticles/reduced graphene oxide composites with excellent microwave absorption performance, *Appl. Surf. Sci.*, 562(2021), art. No. 150212.
[31] F. Wu, M.X. Sun, C.C. Chen, *et al*., Controllable coating of polypyrrole on silicon carbide nanowires as a core–shell nanostructure: A facile method to enhance attenuation characteristics against electromagnetic radiation, *ACS Sustainable Chem. Eng.*, 7(2019), No. 2, p. 2100.
[32] J. Liu, J.P. Zhong, Z.W. Chen, *et al*., Preparation, characterization, application and structure evolution of attapulgite: From nanorods to nanosheets, *Appl. Surf. Sci.*, 565(2021), art. No. 150398.
[33] J. Yan, Q. Zheng, S.P. Wang, *et al*., Multifunctional organic-inorganic hybrid perovskite microcrystalline engineering and electromagnetic response switching multi-band devices, *Adv. Mater.*, 35(2023), No. 25, art. No. e2300015.
[34] X.G. Huang, M. Qiao, X.C. Lu, *et al*., Evolution of dielectric loss-dominated electromagnetic patterns in magnetic absorbers for enhanced microwave absorption performances, *Nano Res.*, 14(2021), No. 11, p. 4006.
[35] G.Y. Tian, W.B. Wang, L. Zong, Y.R. Kang, and A.Q. Wang, From spent dye-loaded palygorskite to a multifunctional palygorskite/carbon/Ag nanocomposite, *RSC Adv.*, 6(2016), No. 48, p. 41696.
[36] W.M. Xie, J. Wang, K.X. Shang, *et al*., A nanoclay-based 3D aerogel framework for flexible flame retardants, *Mater. Adv.*, 3(2022), No. 17, p. 6799.
[37] W. Li, J.P. Yang, Z.X. Wu, *et al*., A versatile kinetics-controlled coating method to construct uniform porous TiO_2 shells for multifunctional core–shell structures, *J. Am. Chem. Soc.*, 134(2012), No. 29, p. 11864.
[38] Z.H. Li, F.H. Liu, G.J. Xu, J.L. Zhang, and C.Y. Chu, A kinetics-controlled coating method to construct 1D attapulgite @ amorphous titanium oxide nanocomposite with high electrorheological activity, *Colloid Polym. Sci.*, 292(2014), No. 12, p. 3327.
[39] T.S. Song, C.Q. Xia, Y.M. Ding, *et al*., Improvement of corrosion and wear resistance of novel Zr–Ti–Al–V alloy with high strength and toughness by thermal nitridation treatment, *Corros. Sci.*, 208(2022), art. No. 110685.
[40] L.X. Gai, L. Guo, Q.D. An, Z.Y. Xiao, S.R. Zhai, and Z.C. Li, Facile fabrication of SBA-15/polypyrrole composites with long-rod shape for enhanced electromagnetic wave absorption, *Microporous Mesoporous Mater.*, 288(2019), art. No. 109584.